IAC-23-A6.1.3

Effects of Phase Angle and Sensor Properties on On-Orbit Debris Detection Using Commercial Star Trackers

Allan Shtofenmakher[a,*], Hamsa Balakrishnan[b]

[a] *Ph.D. Candidate, Department of Aeronautics and Astronautics, Massachusetts Institute of Technology, Cambridge, MA 02139, USA, ashtofen@mit.edu*
[b] *William E. Leonhard (1940) Professor, Department of Aeronautics and Astronautics, Massachusetts Institute of Technology, Cambridge, MA 02139, USA, hamsa@mit.edu*
* Corresponding Author

Abstract

The recent proliferation of resident space objects (RSOs) in low Earth orbit (LEO) threatens the sustainability of space as a resource and requires persistent monitoring to avoid collisions involving valuable space assets. State-of-the-art ground-based space surveillance techniques, due to their susceptibility to atmosphere, weather, and lighting conditions, tend to focus on RSOs with characteristic length greater than 10 cm. Consequently, millions of smaller LEO RSOs remain untracked by ground-based methods, which reduces overall space situational awareness. Onboard satellite sensors offer a space-based method fortracking RSOs. Prior research has investigated the feasibility of using commercial star trackers (CSTs)—optical sensors prevalent on most active spacecraft—to observe, detect, and estimate the position and velocity of RSOs larger than 10 cm. In a recent effort, we expanded on these feasibility studies by assessing the capabilities of CSTs to detect debris particles smaller than 10 cm in characteristic length. In this paper, we extend our previous study by relaxing its zero-phase-angle assumption and characterizing the effect of Sun-RSO-CST phase angle on debris detection range. We identify a number of representative CSTs with publicly available optical characteristics and consider the effects of properties such as pixel pitch, diffraction limit, aperture diameter, and field of view (FOV) on the capability of each CST to detect debris at a given distance and relative velocity (in the form of streak speed). We find that, for debris particles modeled as diffuse Lambertian spheres, Sun-RSO-CST phase angles as high as 57° result in no more than 20% reduction to the useful RSO-CST detection range, and streak speed may serve as a stronger limiting factor for smaller debris particles than for larger ones. Though we identify find a general reduction in the feasible region, the results indicate that CSTs have the potential to substantially enhance space-based debris detection.

Keywords: Space Situational Awareness (SSA); Space-Based Space Surveillance; Orbital Debris Detection; Satellite-Based Optical Sensors; Small Orbital Debris; Apparent Visual Brightness

Nomenclature

A_{opt}	Optical Cross Section
d	Debris Diameter or Characteristic Length
D	Aperture Diameter
f	Focal Length
$F(\phi)$	Phase Function
M	Pixel Count (on One Side of Square Frame)
p	Pixel Pitch
R	RSO-CST Distance or Range
$S_{\max}$	Maximum Streak Speed
V_{cutoff}	AVM Cutoff of CST
V_{rso}	AVM of RSO
V_{sun}	AVM of Sun
θ_R	Angular Resolution (Rayleigh Criterion)
λ	Wavelength (of Light)
ρ	Reflectivity
τ	Exposure Time
ϕ	Phase Angle
ψ	FOV (Along One Side of Square Frame)

Acronyms

AFRL	Air Force Research Laboratory
BST	Berlin Space Technologies
CST	Commercial Star Tracker
FI	Front-Illuminated (CST)
FOV	Field of View
GRD	Ground Resolution Distance
HP	High-Precision (CST)
IADC	Inter-Agency Space Debris Coordination Committee
LEO	Low Earth Orbit
OCS	Optical Cross Section
PSRD	Projected Space Resolution Distance
RSO	Resident Space Object
SNR	Signal-to-Noise Ratio
SSA	Space Situational Awareness
SSN	Space Surveillance Network
ST	Star Tracker
STEM	Science, Technology, Engineering, and Mathematics

1. Introduction and Background

The recent proliferation of resident space objects (RSOs) in low Earth orbit (LEO) threatens the sustainability of space as a resource and requires persistent monitoring to avoid collisions involving valuable space assets [1]. Over 23,000 LEO RSOs—including active satellites, inactive satellites, and non-functional debris—are currently tracked by the U.S. Space Surveillance Network (SSN) [2]. The SSN relies primarily on ground-based space surveillance equipment, such as radar and optical telescopes, which are susceptible to atmosphere, weather, and lighting conditions [3], [4]. These barriers generally limit the focus of state-of-the-art space surveillance methods to RSOs with characteristic length greater than 10 cm, leaving millions of LEO RSOs smaller than 10 cm untracked and uncatalogued [2].

The reduced space situational awareness (SSA) in this regime has had expensive consequences. In December 2022, the Soyuz MS-22 module attached to the International Space Station suffered a coolant leak that rendered the vehicle unsafe to complete its intended mission of returning its crew back to Earth [5]. Instead, the Soyuz MS-23 module was commissioned to replace its damaged counterpart at an estimated launch cost of $80M as a result of this leak, which is suspected to have been caused by an RSO approximately 1 mm in characteristic length [6], [7]. Reducing the risk of further space asset compromise is a priority that requires improved space debris detection and tracking capabilities.

Space-based sensors offer a potential solution to this problem. Unlike their ground-based counterparts, they are generally unaffected by atmosphere, weather, and lighting conditions. Moreover, they tend to be more sensitive and, consequently, can detect smaller and dimmer RSOs [4]. The Space-Based Visible sensor onboard the Midcourse Space Experiment satellite first demonstrated the potential of using onboard satellite sensors to detect and track RSOs in 1998 [8]. Since then, space-based space surveillance has been integral to the SSN's mission, with additional space-based assets deployed every few years [3], [9]. However, the recent, dramatic proliferation of RSOs in LEO, especially when compared to the slow rate of growth in the number of dedicated SSN assets, indicates the need for a far more scalable, widespread, and—ideally—low-cost solution [3].

One promising approach involves the commercial star tracker (CST), an optical sensor used by satellites to determine spacecraft attitude by capturing images of distant stars and comparing them to onboard star catalogs [10]. In addition to stars, these images also often capture incidental RSOs that are within line of sight of the CST and are adequately illuminated by the Sun [10]. With methods such as those proposed by [11] and [12], the positions and velocities of these RSOs can be estimated.

Since the vast majority of currently active satellites feature at least one CST, recent research has investigated the potential for leveraging the thousands of commercial star trackers (CSTs) already on orbit as part of a near-zero-cost distributed space surveillance system [4], [10], [11], [12], [13], [14]. However, the majority of these efforts has focused on improving state estimates for those RSOs that are already tracked by the SSN—that is, those with characteristic length larger than 10 cm in general.

More recently, we have begun investigating the potential for using CSTs to detect and track debris particles *smaller than* 10 cm [14]. We explored the relationship among the apparent visual magnitude (AVM) of the RSO—or the apparent brightness of the RSO as perceived by the observing CST—RSO size, and RSO-CST distance, establishing a parameter space (in terms of the latter two parameters) within which a given CST can feasibly detect debris particles in LEO [14]. In this paper, we relax the zero-phase-angle assumption used in [14] and explore the effect of Sun-RSO-CST phase angle on useful RSO-CST detection range. We also investigate a number of CST sensor characteristics not previously considered, including pixel pitch, angular resolution, and optical field of view (FOV), and describe the constraints they may impose on the feasibility of using CSTs to detect and track RSOs. The theory and methodology for these analyses are presented in Section 2, with key findings depicted and discussed in Sec. 3 and conclusions and recommendations for further research in Sec. 4.

2. Theory and Methodology

This section summarizes the mathematical and physical relationships used to generate the results discussed in Section 3. We first present a mathematical relationship for the AVM of a near-Earth RSO as a function of its optical properties and distance from the observer before presenting a table of representative CSTs and a selection of properties relevant to the overall discussion. We then relax the zero-phase-angle assumption used in earlier research [14] and explore the effects of angular resolution and streak speed, defined in Section 2.5, on detection feasibility.

2.1. Apparent Visual Magnitude for Near-Earth Debris

The ability of a CST to observe an RSO is a function of that RSO's AVM, as viewed by the satellite observer. For RSOs in LEO, this parameter, V_{rso}, can be defined in terms of the AVM of the Sun at Earth, V_{sun}, the distance from the RSO to the observing CST, R, and the object's optical cross section (OCS), A_{opt} [15]:

$$V_{\text{rso}} = V_{\text{sun}} - \frac{5}{2} \log_{10} \frac{A_{\text{opt}}}{R^2} \qquad (1)$$

Eqn. 1 is reverse logarithmic, such that brighter objects have more negative AVM values. In this equation, the AVM of the Sun at Earth is given by $V_{\text{sun}} = -26.5$ [16].

In general, A_{opt} is a time-dependent function of the RSO's geometry, material properties, and angle relative to the Sun and observer. To eliminate this time dependency and simplify optical debris analysis campaigns, the Inter-Agency Space Debris Coordination Committee (IADC) has established a standard in which each orbital debris particle is modeled as a diffuse Lambertian sphere with a phase angle—that is, the Sun-debris-observer or the Sun-RSO-CST angle—of $\phi = 0°$ and a surface reflectivity or albedo of $\rho = 10\%$ [17]. The Lambertian sphere simplification, along with the Barker (2004) model for optical measurements of sunlit near-Earth RSOs, yields the following relationship for the A_{opt} of

a debris particle in LEO [17]:

$$A_{\text{opt}} = \frac{1}{4}\pi d^2 \rho F(\phi) \qquad (2)$$

where, in addition to the already-defined parameters, d represents the diameter of the Lambertian sphere, and $F(\phi)$ is the phase function for the given phase angle, which, according to Williams and McCue [18], is given by:

$$F(\phi) = \frac{2}{3\pi^2}[(\pi - \phi)\cos(\phi) + \sin(\phi)] \qquad (3)$$

Combining Eqns. 1–3 yields a useful relationship for the AVM of a Lambertian debris particle with known size, reflectivity, phase angle with respect to the Sun and observer, and distance from the observer:

$$V_{\text{rso}} = V_{\text{sun}} - \frac{5}{2}\log_{10}\frac{\frac{1}{4}\pi d^2 \rho F(\phi)}{R^2} \qquad (4)$$

It is worth noting that Eqns. 2–4 do not assign any particular value for surface reflectivity or phase angle. However, for the IADC standard model of $\rho = 10\%$ and $\phi = 0°$, the parameter space across debris size, RSO-CST distance, and RSO AVM is explored in detail in [14], with key takeaways summarized in Section 1.

2.2. Representative CSTs and Selected Properties

Several different classes of star tracker (ST) are investigated in [19], which tabulates a variety of parameters for assessing and comparing the respective performance of each imager. Of particular note is the AVM cutoff value, V_{cutoff}, which represents the dimmest AVM that can be detected by a ST for a given signal-to-noise ratio (SNR) and exposure time, τ. Table 1 below presents these three quantities and other relevant parameters for three representative ST classes. The front-illuminated (FI) CST can be considered to represent the class of ST that could be found on a typical microsatellite, whereas the high-precision (HP) CST would represent a comparatively high-end optical sensor, likely custom developed in a laboratory environment, and the nano CST class corresponds to those STs that could be found a low-budget, space-constrained CubeSats and other nanosatellites.

Since [19] assumes square image detector frames and pixels, Table 1 captures the pixel pitch, p, which represents the center-to-center distance between the pixels of the detector array [21], as a single parameter, rather than recording two separate dimensions . Likewise, the size of the detector array is also represented by a single parameter, M, corresponding to the number of pixels on one side of the square detector, and the corresponding FOV along one side of the detector is represented by ψ. The total number of pixels in the detector can be determined by taking the product $M \times M$, and the corresponding square FOV is given by $\psi \times \psi$. Other parameters include the focal length, f, and the aperture diameter, D, of the imager.

Due to continuous improvements in ST and imaging technology, it is likely that the latest generation of CSTs will outperform those imagers investigated in [19], so the information presented in Table 1 can be viewed as conservative.

2.3. Phase Angle and Normalized RSO-CST Range

The zero-phase-angle assumption built into the IADC standard model is most applicable when both the observer and the target RSO pass over the solar terminator while the CST is pointed away from the Sun. Although useful for feasibility assessments, as discussed in [14], this assumption ultimately limits the usefulness of using CSTs to detect and track debris in LEO by restricting this strategy to a fairly niche operating regime. Relaxing the zero phase angle assumption would address this issue and, consequently, increase the generality of the proposed strategy.

We seek to understand the effect of phase angle on RSO-CST detection range. To begin, we express R, the RSO-CST range from Eqn. 4, as an explicit function of the phase function, $F(\phi)$. That is,

$$R \equiv R[F(\phi)] \qquad (5)$$

Solving Eqn. 4 for $R[F(\phi)]$ yields:

$$R[F(\phi)] = \left[\frac{1}{4}\pi d^2 \rho * 10^{-\frac{2}{5}(V_{\text{sun}} - V_{\text{rso}})} * F(\phi)\right]^{\frac{1}{2}} \qquad (6)$$

As discussed in Section 2.2, the dimmest AVM that can be detected by a given CST is given by its V_{cutoff} value. To isolate the effect of phase angle on detection capability, we set V_{rso} in Eqn. 6 above equal to V_{cutoff}, as follows:

$$V_{\text{rso}} \equiv V_{\text{cutoff}} \qquad (7)$$

Using the relationships in Eqn. 6 and Eqn. 7, detection range as a function of phase angle is explored in Section 3.1 for each of the three representative imagers presented in Table 1.

Moreover, for any debris particle modeled as a Lambertian sphere such that ρ and d are fixed, for a given CST with known AVM cutoff value, we can claim that:

$$\left[\frac{1}{4}\pi d^2 \rho * 10^{-\frac{2}{5}(V_{\text{sun}} - V_{\text{cutoff}})}\right]^{\frac{1}{2}} = \text{constant} \qquad (8)$$

Under these conditions, RSO-CST detection range is proportional to the square root of the phase function and is, therefore, ultimately a function of phase angle alone, as shown in Eqn. 9:

$$R[F(\phi)] \propto [F(\phi)]^{\frac{1}{2}} \qquad (9)$$

This enables the normalization of RSO-CST detection range as a function of phase angle with respect to the corresponding (maximum) detection range associated with a phase angle of 0°:

$$\frac{R[F(\phi)]}{R[F(0)]} = \left[\frac{F(\phi)}{F(0)}\right]^{\frac{1}{2}} \qquad (10)$$

This relationship, which is agnostic to debris size, surface reflectivity, sensor sensitivity, and even the brightness of the Sun, is depicted in visual form and discussed further in Section 3.1.

Table 1. Selected properties of representative CSTs/imagers, adapted from [19] unless otherwise stated

CST Type	Example	τ (s)	f (cm)	p (μm)	M	D (cm)	ψ ($°$)	SNR (dB)	V_{cutoff}
HP CST/Imager	MOST [20]	0.1	50	12	1024	6.70	1.41	11	11.1
FI CST	BOKZ-MF	0.1	4	16	512	1.88	11.69	15	6.5
Nano CST	BST ST200	0.1	2	20	256	0.98	14.59	7	4.8

2.4. Diffraction-Limited Angular Resolution

The presence of millions of RSOs in LEO and the fact CSTs can observe multiple RSOs in a single image presents the realistic possibility that two RSOs may be so close to one another in a given snapshot that they appear indistinguishable to the imager [13]. Since distinguishing and uniquely identifying the RSOs observed will be essential for improving the state of the art in tracking of LEO RSOs via space-based sensors, it is useful to quantify this effect and the extent to which it reduces the parameter space for CST-based debris detection. The ability of an optical imager to distinguish two point sources of light—e.g., two LEO RSOs—from one another is quantified by its *angular resolution* [21], [22]. Under ideal conditions, the optimal angular resolution of an optical system corresponds to its *diffraction limit*, which is associated with the physical phenomenon of diffraction, in which light naturally bends as it passes around an obstacle or through an opening, such as the aperture of a CST [22], [23]. For ground-based optical imagers, performance in this regard is often limited by atmospheric distortions than by diffraction limits, but space-based imagers can theoretically operate at their respective diffraction limit if there are no lens aberrations or other camera defects [24]. Assuming the absence of these imperfections, discussed briefly in Section 3.4, most space-based optical systems are capable of producing images with angular resolution at or approaching this theoretical limit and are often described as being diffraction limited [24].

For optical imagers with circular apertures, such as those used in [19] and presented in Table 1, the angular resolution is given by the *Rayleigh criterion*, θ_{R}, which is expressed as a function of light wavelength, λ, and aperture diameter, D, as follows [25], [26]:

$$\theta_{\text{R}} = \arcsin\left(1.2197\frac{\lambda}{D}\right) \quad (11)$$

To translate these angular metrics into more intuitive linear metrics, we must first introduce the concept of *projected space resolution distance* (PSRD). This is defined as the distance between two observed RSOs projected into the image plane, which is perpendicular to the main line of sight of the imager. This is analogous to the concept of ground resolution distance (GRD), which is used in Earth observation applications to denote the distance by which two targets at ground level (e.g., 500 km below the satellite) must be separated in order for the space-based imager to resolve them as distinct features [24]. From basic geometry, the PSRD of a CST with angular resolution θ_{R} observing two RSOs at a distance R from the observer is given, under the small angle approximation, by Eqn. 12:

$$\text{PSRD} \approx R * \theta_{\text{R}} \quad (12)$$

For analysis purposes, if the two RSOs under consideration are at appreciably different distances from the observer, it is recommended to consider the *greater* of the two RSO-CST ranges, as that would yield a higher (i.e., more conservative) PSRD. It is worth noting that the Rayleigh criterion is nominally defined for sources of equal strength—in this case, equal AVM. Thus, a more rigorous investigation into angular resolution involving two RSOs of substantially different AVM is recommended as future work [26]. It is also worth noting that calculations for GRD often consider distortions due to geometric projections and the curvature of the Earth, which reduce the overall resolution capability of the imager [24]. However, in the case of PSRD, if the RSOs are treated as point sources of light, the comparatively simple relationship in Eqn. 12 should hold true.

Eqn. 11 and Eqn. 12 are both explored graphically in Section 3.2 for each of the three represented imagers from Table 1.

2.5. Streak Speed and Field of View

To complement the previous research efforts investigating relative RSO-CST distances for which the observer could successfully detect the target, this section presents the theory and equations for investigating the relative RSO-CST *speeds* for which detection is feasible. One particular concern is *streaking*, which, in astrophotography, refers to the phenomenon by which point sources of light appear as lines or streaks in the resulting image [27]. This tends to happen when the target object is moving with a high *streak speed*, or speed relative to the observer in a direction perpendicular to the axis of the imager (i.e., projected into the image plane), while the image is being taken. A number of strategies have been developed for modeling the light curves from streaks and generating associated RSO position and velocity estimates; however, if the streak speed of the RSO is high enough that the streak spans the entire image and no starting or ending point of the streak can be identified, then position and velocity estimates cannot be generated or are unreliable [11], [13], [27], [28]. A conservative estimate for the maximum allowable streak speed, S_{max}, can therefore be determined from geometric relations.

For the time scales under consideration (on the order of $\tau = 0.1$ seconds), it is reasonable to use linearized dynamics and assume a (momentarily) fixed inertial orientation for the observer spacecraft [24]. Likewise, although the information sourced from [19] and presented in Table 1 assumes "square" FOVs associated with the square detector arrays, the true projection of the FOV onto the spacecraft sky would be slightly larger than is claimed due to the nature of spherical geometry [24]. However, the square FOV parameter captured in Table 1 as ψ offers a lower bound for measuring this projected area, so the results presented in this section can be treated as conservative.

Thus, assuming that the target RSO, streaking in a plane at a distance R from the CST, seeks to traverse the entire CST FOV along the shortest possible path over the CST exposure time, τ, Euclidean trigonometry offers the following relationship:

$$2\tan\left(\frac{\psi}{2}\right) = \frac{S_{\max} * \tau}{R} \qquad (13)$$

Solving Eqn. 13 for the maximum allowable streak speed, $S_{\max}$, yields:

$$S_{\max} = \left[\frac{2\tan\left(\frac{\psi}{2}\right)}{\tau}\right] R \qquad (14)$$

The effect of FOV and distance on maximum allowable streak speed is explored further in Section 3.3 .

3. Results and Discussion

This section presents the main findings of the analyses discussed in Section 2, beginning with the relaxation of the standard IADC zero-phase-angle assumption and the corresponding effects on RSO-CST detection range. This is followed by graphical representations of angular resolution as a function of CST aperture diameter and PSRD and streak speed as functions of RSO-CST distance for each of the three representative CST types discussed in Section 2.2. The section concludes with a discussion of additional, as-yet-unquantified additional limitations, setting the basis for future work.

3.1. Effect of Phase Angle on RSO-CST Detection Range

In this subsection, we identify the effect of phase angle on the maximum distance at which each class of optical imager presented in Table 1 can detect a diffuse Lambertian sphere debris particle with 10% reflectivity and characteristic length of 10 cm. For interested readers, a variety of values for reflectivity and characteristic length can be explored using the methodology discussed in Section 2.

To begin, Fig. 1 offers a graphical visualization of Eqn. 6, with V_{rso} set to the corresponding V_{cutoff} of each representative CST, in turn, to generate each of the three curves.

As predicted by Eqn. 10, the three curves all have similar shapes but different zero-phase-angle ranges. In fact, we find the detection ranges corresponding to $\phi = 0°$ are consistent with the results from the earlier research presented in [14]. Namely, the higher-performing imagers are able to detect 10-cm debris particles with 10% reflectivity over 400 km away. For microsatellite-class and nanosatellite class CSTs, the capability reduces to roughly 50 km and roughly 25 km, respectively. Likewise, although this is not shown in Fig. 1, reducing the debris size to 1 cm reduces the above detection ranges by an order of magnitude, as expected.

As the phase angle grows, the associated detection range decreases—slowly at first before beginning to fall more rapidly after approximately 90°. Nevertheless, the slow initial loss of performance is an attractive result—although phase angle clearly affects detection range and capability, spacecraft are not limited to operation at the solar terminator in order to detect and track LEO RSOs using CSTs.

Fig. 2 further corroborates these claims in its sinusoidal depiction of Eqn. 10. In this figure, the normalized detection range metric is plotted against the phase angle in degrees. Since Eqn. 10 is agnostic to individual CST parameters, only one curve is required.

This data indicates that space-based imagers can be expected to maintain at least 80% of their zero-phase-angle detection range at phase angles as high as 57°. Beyond 90°, however, the performance falls below 57% and rapidly descends thereafter. Regardless, these findings significantly increase the operating envelope for which CST-based RSO detection and tracking will be useful.

3.2. Diffraction Limit and Angular Resolution

In accordance with Eqn. 11, the angular resolution of an optical imager with a circular aperture, as measured by the Rayleigh criterion, is a function of light wavelength and aperture diameter. Most CSTs operate in the range of light wavelengths corresponding to visible light, or approximately 380 nm to 740 nm [29], [30]. For simplicity, this analysis assumes a light wavelength corresponding to the average of these two visible light extremes, or approximately 560 nm, which roughly corresponds to yellow-green visible light.

Thus, Fig. 3 depicts Rayleigh criterion, computed from Eqn. 11, as a function of CST aperture diameter for 560-nm-wavelength light, with dashed vertical lines indicating aperture diameter for the three representative CSTs.

From the intersection of each of the dashed vertical lines with the green angular resolution curve, we can determine the angular resolution associated with each of the three representative CSTs from Table 1. In descending (i.e., improving) order, the nano, micro, and HP CSTs offer angular resolutions of 14.4 arcsec, 7.5 arcsec, and 2.1 arcsec, respectively. As expected from Eqn. 11, for small angles, a two-fold increase in aperture diameter yields a two-fold improvement in angular resolution. In particular, a 0.9-cm increase in aperture diameter from the nano CST to the micro CST results in a 92% (6.9-arcsec) improvement in angular resolution. However, a further 5.4-arcsec improvement in resolution from the micro to the HP CST requires a 256% increase in aperture diameter. Meaningful improvements beyond this point would require significant increases to the size of the instrument or else a shift to a higher-frequency electromagnetic wavelength.

Although not explicitly shown in Fig. 3, the results are fairly sensitive to choice of wavelength, and selecting higher or lower wavelengths worsens or improves (respectively) the angular resolution of each imager proportionally (for small angles). In fact, recent research has investigated custom STs that operate at infrared wavelengths [30]. For example, for imagers operating at 1550 nm, if aperture diameter is unchanged, the angular resolution of each CST would worsen by a factor of 2.8. Once again, interested readers are encouraged to explore a variety of values for wavelength and aperture diameter using the methodology discussed in Section 2.

Since linear distances are more intuitive than angular resolutions, Fig. 4 takes the angular resolutions from Fig. 3 and applies them to Eqn. 12 to generate three
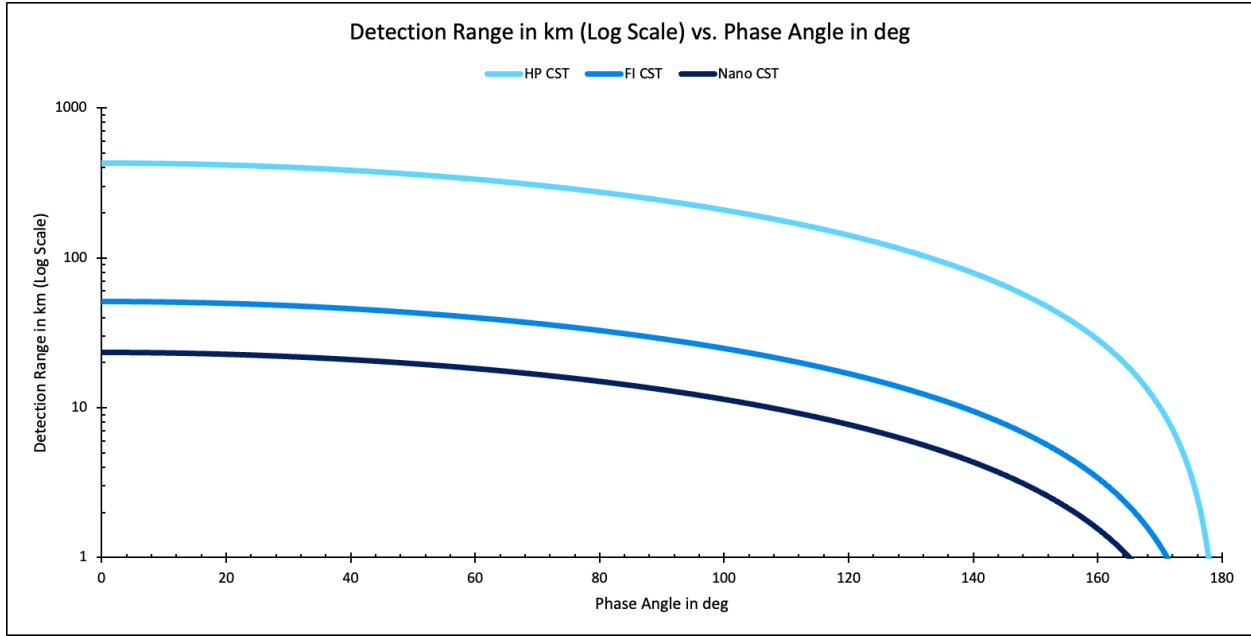
Fig. 1. RSO-CST detection range vs. phase angle for each of the three representative CST classes, using parameters from Table 1, assuming 10-cm debris particles and diffuse Lambertian spheres with 10% reflectivity in accordance with IADC standards [17]
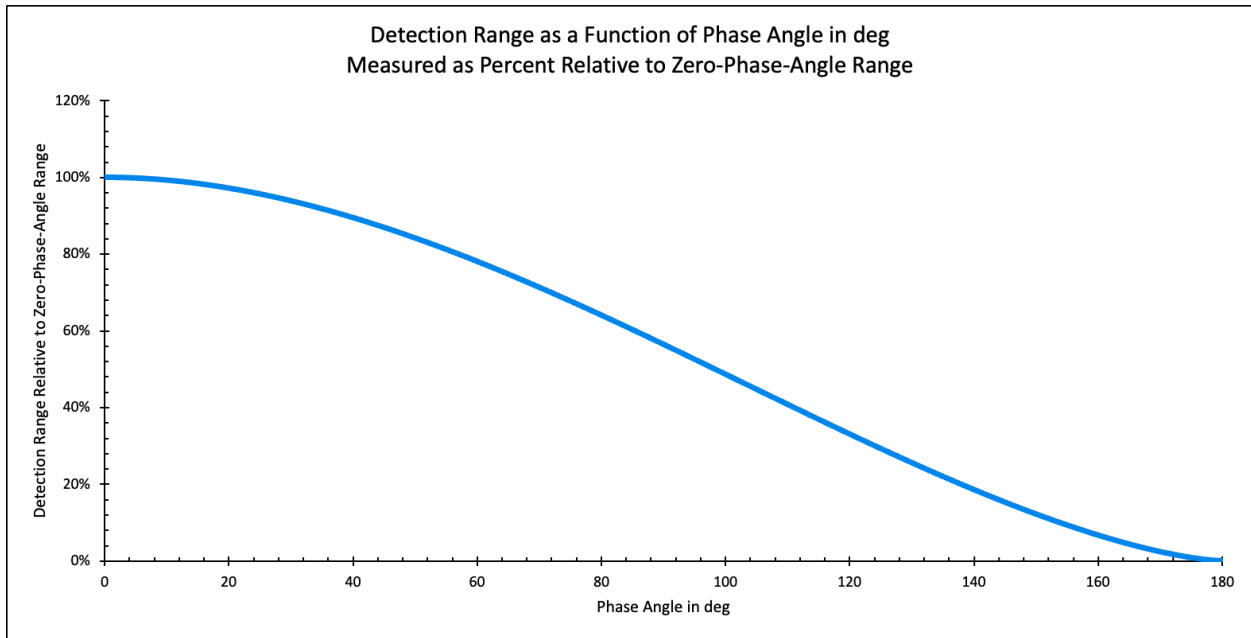

Fig. 2. RSO-CST detection range—expressed as a percent relative to the corresponding detection range at zero phase angle—vs. phase angle, assuming diffuse Lambertian spheres in accordance with IADC standards [17]

individual curves for PSRD vs. RSO-CST range. Due to the small angle approximation, the relationship is essentially linear in all three cases. A horizontal red dashed line is also present to indicate a benchmark RSO-RSO separation value of 10 m, which is comparable to the accuracy at a range of 1000 km of certain ground-based optical telescopes used by the U.S. SSN [31].

Fig. 4 is presented on a log-log scale to show a
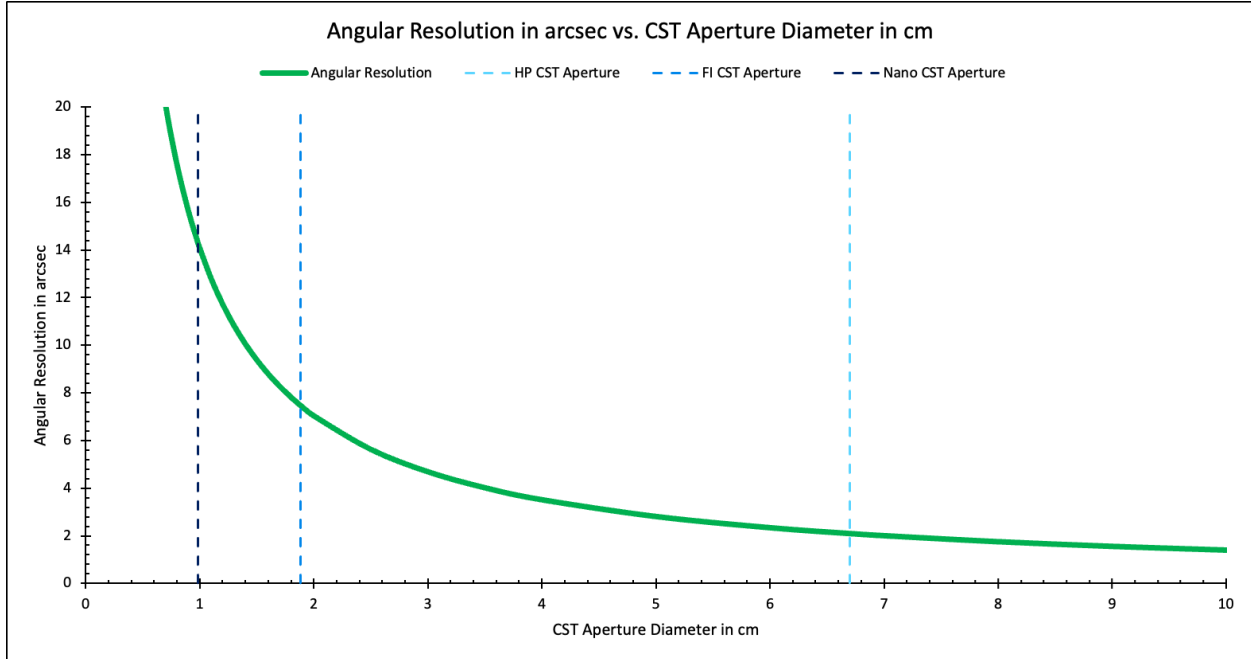
Fig. 3. Angular resolution vs. CST aperture diameter, assuming a visible light wavelength of $\lambda = 560$ nm and circular apertures, with thin vertical lines corresponding to the respective aperture diameters of the three representative CST classes, as presented in Table 1
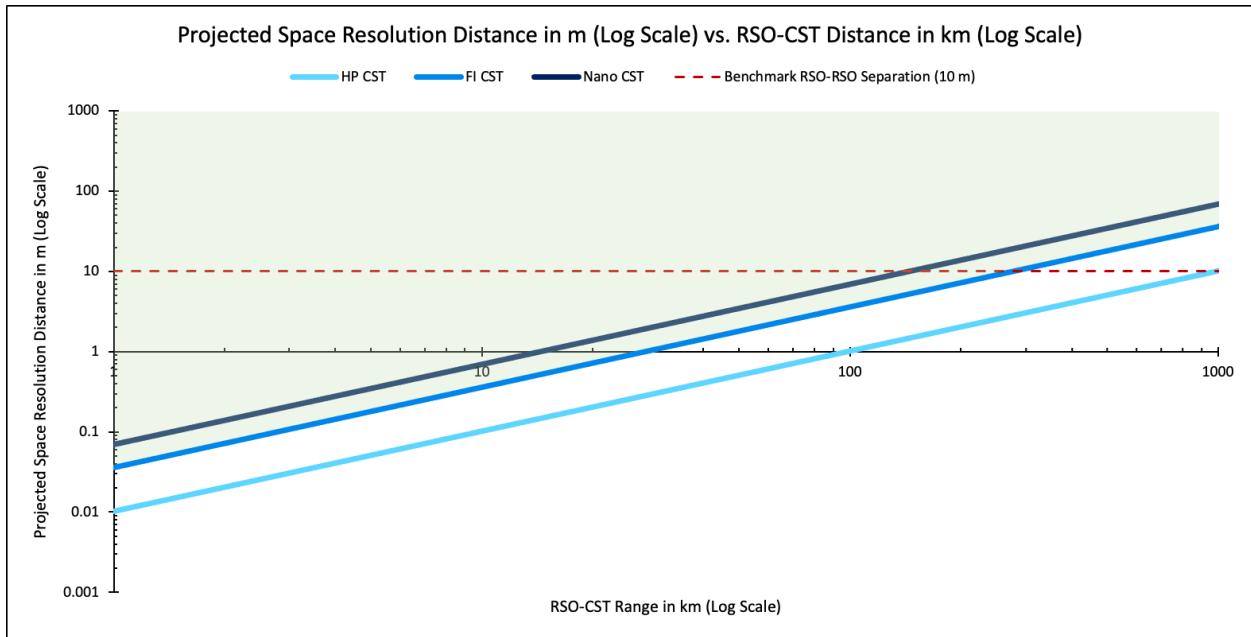

Fig. 4. PSRD vs. RSO-CST range for each of the three representative CST classes, using FOV and integration time parameters from Table 1, with shaded green region representing the parameter space which can be detected by typical microsatellite-class CSTs

broader range of RSO-CST values along the x-axis.
Overall, these results indicate that, for all three CSTs, the angular resolutions from Fig. 3 correspond to PSRDs less than 10 m for RSO-CST ranges as far as 100 km.

In particular, the PSRD of the high-precision imager is approximately 10 m for an RSO-CST range of 1000 km. In other words, the HP CST can resolve two RSOs of comparable AVM 1000 km away as long as they are at least 10 m apart. For comparison, the angular resolution of the tracking and imaging radar operated by the FGAN research institute in Germany is approximately 0.0002°, which corresponds to a PSRD of about 3.5 km at a range of 1000 km [32]. Similarly, the angular accuracy of optical telescopes used by the U.S. SSN can be as high as 5 arcsec, which corresponds to a PSRD of about 12 m at a range of 1000 km [31]. This competitive performance is once again an attractive result showcasing the potential capability of space-based debris detection and tracking using CSTs.

3.3. Effect of Streak Speed on Detection Capability

It is a well-established fact that RSOs captured in CST images tend to appear as streaks, and recent research has investigated methods for successfully estimating RSO position and velocity from these streaks [11], [13], [27], [28], [33]. The goal of this subsection is establish a benchmark maximum streak speed for objects in LEO and to investigate and visualize the effect of FOV and RSO-CST range on the maximum streak speed that is allowable in accordance with Eqn. 14.

In theory, objects merely visiting LEO may be traveling at arbitrarily high velocities when they are imaged by a CST. In general, however, the majority of LEO RSOs reside in low-eccentricity or near-circular orbits [24], and the fastest theoretical speed that an RSO in a circular Earth orbit can attain is approximately 7.905 km/s, which corresponds to the speed of a satellite orbiting Earth at an altitude of 0 km above ground [24]. To set a reasonable upper bound for streak speed, we consider a situation in which the target RSO and the CST are (momentarily) moving at this theoretical maximum speed in antiparallel directions at the instant of imaging. In this case, the benchmark streak speed is given by:

$$S_{\mathrm{max,benchmark}} = 2\left(7.905\frac{\mathrm{km}}{\mathrm{s}}\right) = 15.810\frac{\mathrm{km}}{\mathrm{s}} \quad (15)$$

This benchmark represents the maximum streak speed, in theory, that a CST could encounter in its quest to detect LEO RSOs and is captured in Fig, 5, which depicts maximum detectable streak speed vs. RSO-CST range for each of the three representative CSTs from Table 1 according to Eqn. 14, as a horizontal dashed red line.

The intersection of the horizontal dashed red line with each of the diagonal blue lines yields the *minimum* RSO-CST range, above which any images taken by that particular CST should include at least one endpoint of the streak of a target LEO RSO. The only exception to this finding would be any LEO RSOs that are streaking at speeds in excess of 15.810 km/s, which, as discussed above, is highly unlikely.

In a deviation from most of the other findings in this paper and in [14], the HP CST does *not* outperform the other representative imagers with regards to maximum detectable streak speed. In ascending (i.e., improving) order, the HP, micro, and nano CSTs would be able to image the full streak of a LEO RSO traveling at $S_{\mathrm{max,benchmark}}$ at RSO-CST ranges of at least 24 km, 84 km, and 161 km, respectively. Ultimately, given the narrow FOV of the HP CST, this is a logical result and serves as a meaningful limitation on the capability of HP CSTs to detect high-streak-speed objects.

The physics involved in Eqn. 14 are largely independent of debris size. However, as discussed in [14], in order to detect smaller debris, the range between object and observer generally must be reduced to compensate for the reduced AVM of the target RSO. Fig. 5 indicates that, in such cases, the feasible parameter space for debris detection is constrained by maximumum detectable streak speed.

For example, [14] found that nano CSTs could detect 1-cm debris out to approximately 2.5 km (assuming zero phase angle). From Fig. 5, this corresponds to a maximum detectable streak speed of approximately 5.8 km/s, which is appreciable less than the theoretical maximum benchmark streak speed establish in Eqn. 15. Thus, at such distances, some RSOs may reasonably be traveling with relative velocities the preclude proper detection by the CST. Combining this result with those of Section 3.1, for higher phase angles, the maximum detectable RSO-CST range for a given RSO would be further reduced, which, in turn, corresponds to a lower detectable streak speed.

For proper investigation of the coupling of these various constraints and their intersectional effects on the feasible parameter space for CST-based RSO detection and tracking, we recommend the development and analysis of detailed simulations as future work.

3.4. Additional Limitations

Beyond the limiting factors and constraints already discussed in Section 2 and Section 3, we briefly consider a number of additional qualitative and quantifiable (but as-yet unquantified) constraints on CST-based RSO detection performance.

One of the primary qualitative limitations in this regard is not physical but logistical in nature. In particular, an appreciable fraction of CSTs that are currently on orbit do not generally save any images taken during nominal operation; instead, they output attitude information (e.g., quaternions) directly to the spacecraft flight computer, discarding any RSO-related information in the process [34]. Changing this behavior en masse for all affected on-orbit CSTs would likely require patches to spacecraft software or CST firmware, which is unlikely—if not impossible—without mass collaboration from the aerospace industry. Although it may be possible to bypass any need for saving images by using onboard RSO detection or state estimation algorithms, as discussed in [33], widespread software or firmware patches would be required in any case. However, with enough progress and interest in the field of space-based space surveillance, it may be possible to change this behavior for future space missions.

It has also been hypothesized that simultaneous attitude determination and RSO recognition will burden the computers onboard participating spacecraft [33]. However, researchers have been investigating this issue for several years now and have developed lightweight algorithms for onboard RSO detection with minimal effect on
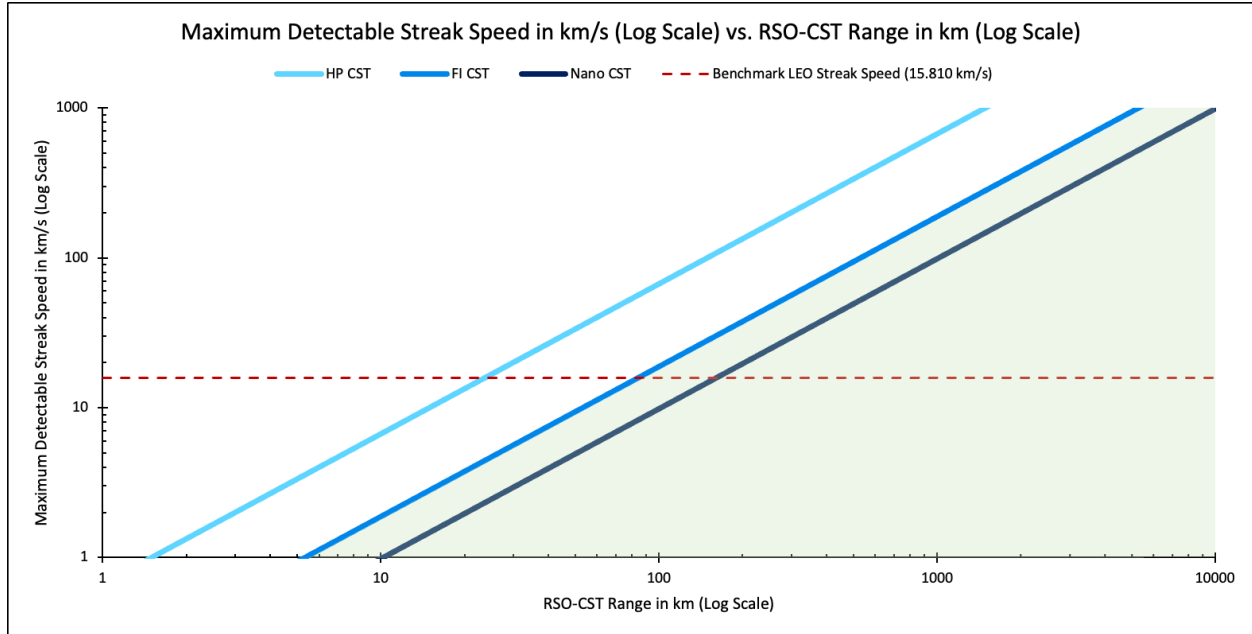
Fig. 5. Maximum detectable streak speed vs. RSO-CST range for each of the three representative CST classes, using parameters from Table 1, assuming a visible light wavelength of $\lambda = 560$ nm and circular apertures, with shaded green region representing the parameter space which can be detected by typical microsatellite-class CSTs

required CST and spacecraft computational power [11], [33].

Furthermore, aberrations in the star tracker lens generally reduce their effectiveness in detecting and tracking illuminated space objects [19]. In particular, [24] identifies chromatic and spherical aberrations, coma, astigmatism, distortion, and curvature of field as some of the principal aberrations that tend to reduce performance in optical system. Although optical aberration theory is a mature field, quantifying these limitations and their effects on the feasible parameter space for CST-based detection of RSOs is identified as future work [19].

4. Conclusions and Future Work

In this paper, we expanded on analysis presented in previous research indicating that CSTs can be used to detect orbital debris particles between 1 cm and 10 cm in diameter up to specified distances [14] by investigating additional parameters that may limit the usefulness of CST-based debris detection. In addition to the CST AVM cutoff values investigated previously, we studied non-zero phase angles, pixel pitch, angular resolution, aperture diameter, and FOV. As before, the debris particles were modeled in accordance with IADC standards and and treated as diffuse Lambertian spheres with 10% surface reflectivity. The Barker (2004) model, defined for optical measurements of sunlit RSOs near Earth objects, was used to relate the AVM of the RSOs to their characteristic length, phase angle, and distance from the observer. A series of three representative imagers was identified to characterize the effects of their various optical and geometric properties on CST-based RSO detection capability [19]. The traditional zero-phase-angle assumption of the IADC standard model was relaxed in order to investigate the effect of phase angle on RSO-CST detection range. The ability of the selected CSTs to resolve two RSOs in the same image (i.e., angular resolution) and to detect streaking RSOs was likewise investigated to characterize any potential limitations associated with angular (and, by extension, projected linear) resolution and relative RSO-CST velocity. The discussion concluded with a brief discussion of other limiting factors.

The overall results are generally favorable with regards to the use of CSTs to detect space debris and identify a series of additional parameters to consider for accurate simulation and assessment of space-based debris detection via CSTs. In particular, as shown in Fig. 1, relaxing the previous zero-phase-angle assumption only reduces the useful RSO-CST detection range by 20% for phase angles up to 57°. Moreover, we find that the dependence on phase angle is independent of other RSO and CST parameters under consideration when the RSO-CST detection range is normalized by the corresponding zero-phase-angle range, per Eqn. 3 and Fig. 2.

We likewise find that, for the RSO-CST ranges over which CST-based detection of LEO debris would be useful, angular resolution is not a significant limiting factor. This conclusion was supported by translating the Rayleigh criterion findings from Fig. 3 into more intuitive linear distances represented by PSRD values in Fig. 4. In practice, however, for the purposes of assessing correlation confidence in a space-based debris detection simulation, it is more useful to investigate angular resolution than PSRD, as the RSO-CST range for the two RSOs may differ significantly.

The investigation into the relationship between FOV and streak speed and FOV revealed the limitations of CST-based RSO detection capability. For example, smaller FOVs are associated with lower maximum allowable streak speeds, all else being equal. This effect is particularly noticeable for smaller (and dimmer) objects, which, as discussed in [14], can only be detected at comparatively small RSO-CST distances. Ultimately, this does not eliminate the possibility of detection, but it does serve as a useful constraint for any future simulation work that will leverage space-based optical sensors for debris detection. Moreover, a general trend among the three CST classes explored indicates that a higher AVM cutoff correlates with a lower FOV. Thus, although these higher-precision CSTs can generally observe small debris particles at a given distance, they are limited in the volume of space they can scan and the relative velocity of the RSOs they can detect. More rigorous simulation work is required to assess the overall performance of these HP CSTs relative to the microsatellite- and nanosatellite-class CSTs with regards to improving SSA.

Another promising direction for further study is investigating angular resolution relationships between two RSOs of substantially different AVM, since the Rayleigh criterion definition nominally applies to light sources of equal brightness [26]. In addition, quantifying the effects of optical aberrations and other imager imperfections RSO-CST detection range and AVM cutoff values would provide additional practical constraints on the usefulness of leveraging CSTs for detecting debris.

Acknowledgments

References

[1] R. Hiles, A. Alexander, N. Herzer, D. McKissock, A. Mitchell, J. Sapinoso, Report on 2020 mega-constellation deployments and impacts to space domain awareness, in: Advanced Maui Optical and Space Surveillance Technologies Conference, Maui, HI, 2021.
URL https://amostech.com/Technical Papers/2021/SSA-SDA/Hiles.pdf

[2] K. L. Hobbs, A. R. Collins, E. M. Feron, Towards a taxonomy for automatic and autonomous cooperative spacecraft maneuvering in a space traffic management framework, in: AIAA ASCEND, 2020.
URL https://doi.org/10.2514/6.2020 -4240

[3] B. Weeden, Space situational awareness fact sheet, Online, accessed: 2023-07-20 (May 2017).
URL https://swfound.org/media/2058 74/swf_ssa_fact_sheet.pdf

[4] B. Lal, A. Balakrishnan, B. M. Caldwell, R. S. Buenconsejo, S. A. Carioscia, Global trends in space situational awareness (SSA) and space traffic management (STM), Tech. Rep. D-9074, Log H 18-000179, Institute for Defense Analyses Science and Technology Policy Institute, Washington, DC (April 2018).
URL https://apps.dtic.mil/sti/pdfs /AD1123106.pdf

[5] B. Tingley, Russia releases 1st images of damage to leaky soyuz spacecraft (photos), accessed: 2023-12-15 (February 2023).
URL https://www.space.com/soyuz-s pacecraft-leak-photos-russia-spa ce-agency

[6] Space Launch Schedule, Soyuz MS-23: Soyuz 2.1a, accessed: 2023-09-14 (February 2023).
URL https://www.spacelaunchsched ule.com/launch/soyuz-2-1a-soyuz-m s-23/

[7] E. Howell, Russia's 'final decision' on leaky soyuz spacecraft at space station to come in january: reports, accessed: 2023-12-15 (December 2022).
URL https://www.space.com/russia-l eaky-soyuz-decision-january-2023

[8] J. Sharma, G. H. Stokes, C. von Braun, G. Zollinger, A. J. Wiseman, Toward operational space-based space surveillance, Lincoln Laboratory Journal 13 (2) (2002) 309–334.
URL https://archive.ll.mit.edu/pub lications/journal/pdf/vol13_no2/13 _2spacesurveillance.pdf

[9] Air Force Space Command, Space based space surveillance, Online, accessed: 2023-07-20 (July 2019).
URL https://www.afspc.af.mil/About -Us/Fact-Sheets/Article/249017/s pace-based-space-surveillance/

[10] M. Liu, H. Wang, H. Yi, Y. Xue, D. Wen, F. Wang, Y. Shen, Y. Pan, Space debris detection and positioning technology based on multiple star trackers, Applied Sciences 12 (7) (April 2022).
URL https://doi.org/10.3390/app120 73593

[11] S. Dave, R. Clark, G. Chianelli, R. Lee, Machine learning implementation for in-orbit RSO orbit estimation using star tracker cameras, in: Advanced Maui Optical and Space Surveillance Technologies Conference, Maui, HI, 2022.
URL https://amostech.com/Technical Papers/2020/Machine-Learning-App lications-of-SSA/Dave.pdf

[12] S. Dave, R. Lee, RSO position and velocity estimation using convolutional neural networks from

in-orbit star tracker images, in: 43rd Committee on Space Research Scientific Assembly, 2021.

[13] S. Clemens, R. Lee, P. Harrison, W. Soh, Feasibility of using commercial star trackers for on-orbit resident space object detection, in: Advanced Maui Optical and Space Surveillance Technologies Conference, Maui, HI, 2018.
URL https://amostech.com/Technical Papers/2018/Space-Based_Assets/Clemens.pdf

[14] A. Shtofenmakher, H. Balakrishnan, Feasibility analysis of on-orbit debris detection using commercial star trackers, in: IAA Space Traffic Management Conference, Austin, TX, 2023.
URL https://web.tresorit.com/l/b2c gc#8T1h86yuZ2SdwScwfc_vtA&viewer=P RWRtmo2rg8agY3sFb9x0QCirmMkiMKV

[15] J. T. McGraw, M. R. Ackermann, P. C. Zimmer, J. B. Martin, Blind search for micro satellites in LEO: Optical signatures and search strategies, in: Advanced Maui Optical and Space Surveillance Technologies Conference, Maui, HI, 2003.

[16] M. Driedger, P. Ferguson, Feasibility study of an orbital navigation filter using resident space object observations, Journal of Guidance, Control, and Dynamics 44 (3) (2020) 622–628.
URL https://doi.org/10.2514/1.G005 210

[17] J. Africano, P. Kervin, D. Hall, P. Sydney, J. Ross, T. Payne, S. Gregory, K. Jorgensen, K. Jarvis, T. Parr-Thumm, G. Stansbery, E. Barker, Understanding photometric phase angle corrections, in: Proceedings of the Fourth European Conference on Space Debris, Darmstadt, Germany, 2005, pp. 141–146.
URL https://articles.adsabs.harvar d.edu/pdf/2005spde.conf..141A

[18] J. G. Williams, G. A. McCue, An analysis of satellite optical characteristics data, Planetary and Space Science 14 (9) (1966) 839–847.
URL https://doi.org/10.1016/0032-0 633(66)90090-0

[19] A. I. Zakharov, M. E. Prokhorov, M. S. Tuchin, A. O. Zhukov, Minimum star tracker specifications required to achieve a given attitude accuracy, Astrophysical Bulletin 68 (4) (2013) 481–493.
URL https://doi.org/10.1134/S19903 4131304010X

[20] S. Rucinksi, K. Carroll, R. Kuschnig, J. Matthews, P. Stibrany, MOST (Microvariability & Oscillations of Stars) Canadian astronomical micro-satellite, Advances in Space Research 31 (2) (2003) 371–373.
URL https://doi.org/10.1016/S027 3-1177(02)00628-2

[21] G. Verhoeven, Resolving some spatial resolution issues, AARGnews: Newsletter of the Aerial Archaeology Research Group 57 (6) (2018) 25–34.
URL https://core.ac.uk/download/pd f/188647129.pdf

[22] A. G. Hayes, P. Corlies, C. Tate, M. Barrington, J. Bell, J. N. Maki, M. Caplinger, M. Ravine, K. M. Kinch, K. Herkenhoff, B. Horgan, J. Johnson, M. Lemmon, G. Paar, M. S. Rice, E. Jensen, T. M. Kubacki, E. Cloutis, R. Deen, B. L. Ehlmann, E. Lakdawalla, R. Sullivan, A. Winhold, A. Parkinson, Z. Bailey, J. van Beek, P. Caballo-Perucha, E. Cisneros, D. Dixon, C. Donaldson, O. B. Jensen, J. Kuik, K. Lapo, A. Magee, M. Merusi, J. Mollerup, N. Scudder, C. Seeger, E. Stanish, M. Starr, M. Thompson, N. Turenne, K. Winchell, Pre-flight calibration of the Mars 2020 rover Mastcam Zoom (Mastcam-Z) multispectral, stereoscopic imager, Space Science Reviews 217 (29) (2021) 1–95.
URL https://doi.org/10.1007/s11214 -021-00795-x

[23] C. R. Nave, Diffraction, accessed: 2023-09-14 (May 2018).
URL http://hyperphysics.phy-astr. gsu.edu/hbase/phyopt/diffracon.htm l

[24] J. R. Wertz, D. F. Everett, J. J. Puschell, Space Mission Engineering: The New SMAD, Space Technology Library; v. 28, Microcosm Press, Hawthorne, CA, 2011.

[25] C. R. Nave, The Rayleigh criterion, accessed: 2023-09-14 (September 2018).
URL http://hyperphysics.phy-astr. gsu.edu/hbase/phyopt/Raylei.html

[26] Lord Rayleigh F.R.S., Investigations in optics, with special reference to the spectroscope, The London, Edinburgh, and Dublin Philosophical Magazine and Journal of Science 8 (49) (1879) 261–274.
URL https://doi.org/10.1080/147864 47908639684

[27] L. Varela, L. Boucheron, N. Malone, N. Spurlock, Streak detection in wide field of view images using convolutional neural networks (CNNs), in: Advanced Maui Optical and Space Surveillance Technologies Conference, Maui, HI, 2019.
URL https://amostech.com/Technical Papers/2019/Machine-Learning-for -SSA-Applications/Varela.pdf

[28] R. Linares, R. Furfaro, Space object classification using deep convolutional neural networks, in: 19th International Conference on Information Fusion, Heidelberg, Germany, 2016.
URL https://ieeexplore.ieee.org/do cument/7528013

[29] D. Malacara, Color Vision and Colorimetry: Theory and Applications, Second Edition, SPIE Press, Bellingham, WA, 2011.

[30] A. J. Swank, SWIR star tracking, Tech. Rep. NASA/TM-20220007061, NASA Glenn Research Center, Cleveland, OH (May 2022).
URL https://ntrs.nasa.gov/api/cita tions/20220007061/downloads/TM-2 0220007061.pdf

[31] L. Chen, X.-Z. Bai, Y.-G. Liang, K.-B. Li, Orbital Data Applications for Space Objects, Springer Singapore, Singapore, 2016.

URL `https://doi.org/10.1007/978-9` `81-10-2963-9`

[32] J. R. Alarcón, H. Klinkrad, J. Cuesta, F. M. Martinez, Independent orbit determination for collision avoidance, in: Proceedings of the Fourth European Conference on Space Debris, Darmstadt, Germany, 2005, pp. 331–336.
URL `https://conference.sdo.esoc.es` `a.int/proceedings/sdc4/paper/77/SD` `C4-paper77.pdf`

[33] D. Spiller, E. Magionami, V. Schiattarella, F. Curti, C. Facchinetti, L. Ansalone, A. Tuozzi, On-orbit recognition of resident space objects by using star trackers, Acta Astronautica 177 (2020) 478–496.
URL `https://doi.org/10.1016/j.acta` `astro.2020.08.009`

[34] D. Sinclair, C. Grant, Star Tracker ST-16RT2 Interface Control Document, Sinclair Interplanetary by Rocket Lab, Toronto, Canada, rev. 1.32, Accessed: 2023-09-14 (April 2021).
URL `https://www.rocketlabusa.com/a` `ssets/Uploads/RL%20-%20Star%20Tra` `cker%20-%20ICD.pdf`